Turbulent Dynamics of a Submarine Spring Plume

***Sam Aucoin*, Alex Hay, Ruth Musgrave**

Department of Oceanography, Dalhousie University, Halifax, NS, Canada

sam.aucoin@dal.ca

1. Submarine Springs and Plumes

Submarine groundwater discharge (SGD) refers to the seepage of subterranean water into the ocean. The discharge fluid is characterized by the presence of fresh groundwater (Fig. 1), and is therefore generally buoyant.

For seeps that are sufficiently close to a point source, the discharge forms a buoyant plume (Fig. 2, 3), and is termed a submarine spring. These buoyant plumes act as efficient mixing mechanisms generated by the discharge itself.

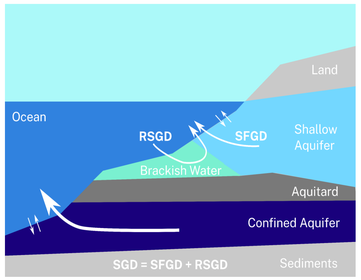

Figure 1: Schematic of submarine groundwater discharge. Shallow aquifers tends to lead to diffuse discharge, while confined aquifers have the extra pressure needed to create point-source springs. The discharge fluid is an unknown mixture of submarine fresh groundwater (SFGD) and recirculated saline groundwater discharge (RSGD).

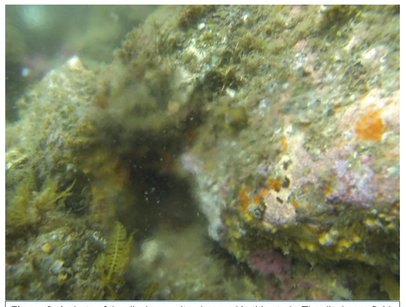

Figure 2: A photo of the discharge site observed in this study. The discharge fluid can be seen by the scintillation caused by variations in the index of refraction of the mixing fresh and saline water, particularly visible in the center-left.

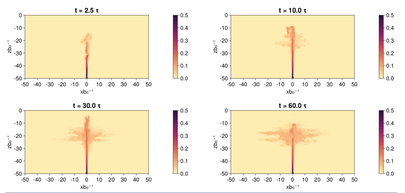

Figure 3: A numerical simulation showing the initial stages of the formation of a buoyant plume, visualized by the arbitrary concentration of a passive tracer. Here, the axes are non-dimensionalized by the source radius, $\mathbf{b_0}$, and time by $\boldsymbol{\tau = z_{max}/w_{max}}$. The instabilities inherent in the plume lead to high levels of turbulent mixing.

2. Field Site

The studied submarine spring is located approximately 1.5 m deep, 5-10 m from shore in a bay in the western part of the Seto inland sea, in Hiji, Oita prefecture, Japan (see Fig. 4). Being in a very rocky area, the exact size of the discharge is difficult to determine, since many small seeps appear between the rocks. The seep chosen for the study of its plume was determined to have the largest discharge volume and is approximately 10-20 cm in diameter (see videos below).

A simple float containing a 5-beam Nortek Signature 1000 ADCP, a CTD and a downward-facing camera was three-point moored overtop of the plume for approximately 90 minutes during low tide (see Fig. 5). The ADCP was configured to run with a **4 Hz** sample frequency in Nortek's "HR mode" with **5 cm** bins in all 5 beams, giving an extended ambiguity velocity of **~1.5 m s^{-1}** (Shcherbina et al., 2018).

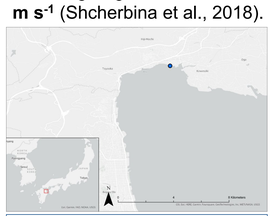

Figure 4: A map of the field site. The spring (blue dot) is located in a bay in the western part of the Seto inland sea in Hiji, Oita prefecture, Japan.

Videos of the spring here!

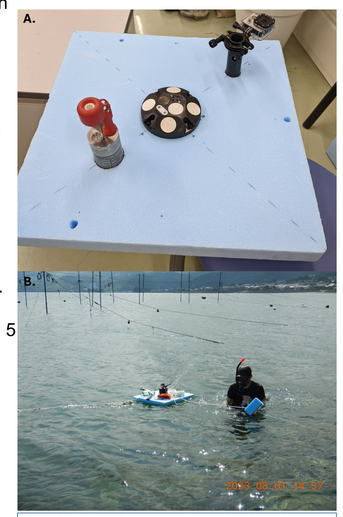

Figure 5: A. The underside of the float used for data collection. A five-beam Nortek Signature 1000 ADCP is in the centre with a removable RBR Brevio CTD to its left, and a downward-facing camera to its right. **B.** The ADCP float deployed over the fresh submarine spring in Hiji, Japan.

3. Removing the Surface Wave Signature

We are interested in the mixing dynamics of the submarine spring plume. Its velocity signature is $O(0.1)$ m s^{-1}, thus even the small amplitude surface waves present during the field study are a significant source of velocity contamination (Fig. 6). Decomposing the velocity time series of each beam, U_b with

$$U_b = U_b^{ADCP} + U_b^{wave} + U_b', \qquad (1)$$

We want to remove the along-beam artificial velocity introduced by the motion of the ADCP, U_b^{ADCP}, and the wave-induced velocity U_b^{wave} , to isolate the other, turbulent velocity signals, U_b'.

U_b^{ADCP} is simply taken to be the motion of the seafloor in each corresponding beam.

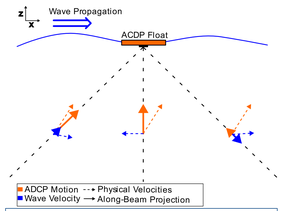

Figure 6: A schematic of the effect of wave-related sources of contamination (dotted lines) on the measured velocities (solid lines). The ADCP motion (orange lines) and wave-induced velocities (blue lines) have a unique combination for each range cell of each beam.

U_b^{wave} is reconstructed using linear wave theory; to do so, the **amplitude**, **frequency** and **phase** of the waves must be constrained.

We obtain these from the time series of the vertical velocity of the ADCP float, W^{ADCP}, taken as the 5-beam average of the estimates of the vertical velocity of the seafloor.

W^{ADCP} is decomposed into time series of its characteristic oscillations using intrinsic mode functions (IMFs) (Huang et al. 1998, see Fig. 7).

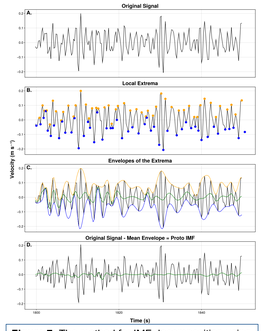

Figure 7: The method for IMF decomposition using an example subset of the data. **A.** The input time series; **B.** the local maxima (orange) and minima (blue) are found; **C.** a cubic spline is separately fit for the maxima and minima, and the average of their envelope is calculated (green); **D.** the average envelope is subtracted from the input data, and the result (black line) is a proto-IMF. The average envelope in **D.** (green line) is still non-zero, thus the above is repeated on the proto-IMF until it is sufficiently close to zero, giving one IMF. The resulting IMF is then subtracted from the input data, and the whole algorithm is repeated to obtain the next IMF. The process stops when the resulting time series does not complete a full oscillation, making it the mean trend.

The IMFs are then individually Hilbert transformed, allowing us to analytically represent the original time series as a sum of N IMFs with amplitude A_j and frequency Ω_j (see Fig. 8):

$$W^{ADCP}(t) = \sum_{j=1}^{N} A_j(t) \exp\left[i \int \Omega_j(t) dt \right]. \qquad (2)$$

(2) is finally taken as the $z = 0$ boundary condition to solve for the analytical wave velocity field, the result of which is projected into beam coordinates and removed from U_b (Fig. 9, 10).

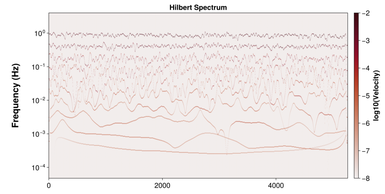

Figure 8: Hilbert-Huang spectrum of W^{ADCP}. Each line represents the amplitude and frequency content of one IMF. The first two IMFs are unequivocally wave-related, being the most stable and energetic, and are therefore used to reconstruct the wave field using linear wave theory.

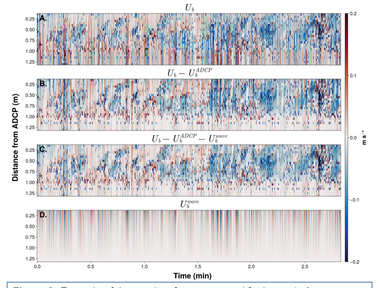

Figure 9: Example of the results of wave removal for beam 1. **A.** unmodified along-beam velocity; **B.** motion of the ADCP removed; **C.** motion of the ADCP and the wave-induced velocities removed; **D.** the along-beam reconstructed wave velocity. Note that negative velocities are upward, since the ADCP was in a downward-looking configuration.

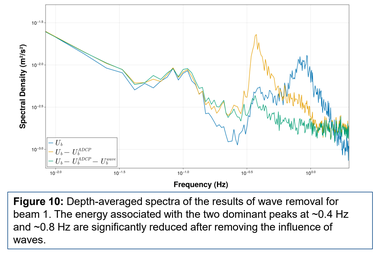

Figure 10: Depth-averaged spectra of the results of wave removal for beam 1. The energy associated with the two dominant peaks at ~0.4 Hz and ~0.8 Hz are significantly reduced after removing the influence of waves.

4. Estimating the Turbulence Field

A first step in quantifying the mixing associated with submarine springs is to quantify the turbulence. This can be accomplished using structure functions to describe velocity correlations D_{LL} in terms of the dissipation of turbulent kinetic energy rate ε (Kolmogorov, 1941):

$$D_{LL}(z,r,\bar{t}) \equiv \left\langle \left(u'(z,t) - u'(z+r,t) \right)^2 \right\rangle = C\varepsilon(z,\bar{t})^{2/3} r^{2/3} \qquad (3)$$

where u' is the demeaned velocity in the direction of separation r at time t, C is the Kolmogorov universal constant, taken to be 2.0 (Sreenivasan, 1995), and the angle brackets denote a time average, giving subsampled time $\bar{t}$.

D_{LL} is calculated for different values of r, up to a maximum r_{max}, representing the limit of homogeneity of the turbulence. Three different methods for estimating D_{LL} are used; a centered differencing approach, considering r both above and below z (Wiles et al., 2006); an upward approach only considering r above z; and a downward approach only considering r below z (Fig. 12).

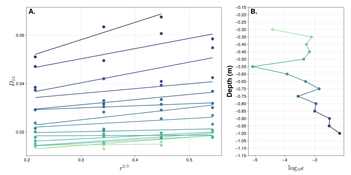

Figure 11: An example of the calculation to estimate ε profiles for beam 5. **A.** linear fits to D_{LL}; each colour/line represents one depth. Each estimate of D_{LL} is taken as an average over ~8 minutes of data in this instance, and a max separation of 0.4 m is used. **B.** The profile of ε estimates from the slopes in **A.**

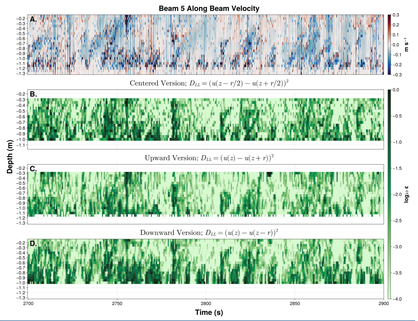

Figure 12: Comparison of three different methods of calculating ε profiles with a subset of beam 5 along beam velocity. Estimates of ε are interpolated with a 2D cubic spline fit for visualization. The estimates of ε map well onto the measured velocities. Each calculation method give qualitatively similar results, but each is biased in a different way. As r_{max} is decreased, the three methods become more similar; here we use a maximum separation of 0.3 m.

Regardless of the estimation method used, D_{LL} is fit to (3) with

$$D_{LL}(z,r,\bar{t}) = \mathrm{N}(z) + \mathrm{A}(z,\bar{t}) r^{2/3} \qquad (4)$$

where $\varepsilon(z,\bar{t}) = \left(\frac{\mathrm{A}(z,\bar{t})}{C}\right)^{3/2}$ (see Fig. 11, 13), and $\mathrm{N}(z) = 2\sigma_{ei}(z)^2$ is an offset from the Doppler noise variance ${\sigma_{ei}}^2$ (see Fig. 14).

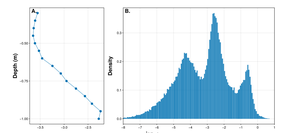

Figure 13: A. log average profile and **B.** probability density distribution of estimates of ε using the centered differencing approach. ε increases with depth, closer to the source of the spring. Three peaks are visible in **B.**, likely due to the distinct turbulence conditions in and out of the plumes.

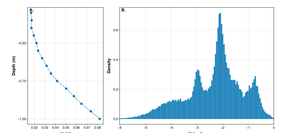

Figure 14: A. Average profile and **B.** probability density distribution of the ADCP Doppler noise variance, σ_{ei}, estimated from the intercept of the structure function fits (4) using the centered approach in Fig. 12. Negative estimates of σ_{ei} are discarded as unphysical. The variance increases with depth associated with signal decorrelation likely caused by a combination of increasing turbulence levels as in Fig. 13 **A.**, and an increasing sample volume with range due to beam divergence (Shcherbina et al., 2018).

5. Next Steps

Future work will determine the most statistically robust estimation method for ε given the high heterogeneity and small scales, as well as make further comparisons to existing plume theory.

Further work will also include large eddy simulations of the field site, using Oceananigans (Ramadhan et al., 2020), to compare observations to an idealized spring.

These two avenues will be used to quantify the turbulent entrainment and mixing of the spring water to interpret the impact of submarine groundwater on the coastal environment.

References

Huang, N. E., Shen, Z., Long, S. R., Wu, M. C., Shih, H. H., Zheng, Q., Yen, N.-C., Tung, C. C., & Liu, H. H. (1998). The Empirical Mode Decomposition and the Hilbert Spectrum for Nonlinear and Non-Stationary Time Series Analysis. *Proceedings: Mathematical, Physical and Engineering Sciences*, *454*(1971), 903–995.

Kolmogorov, A. N. (1941). LOCAL STRUCTURE OF TURBULENCE IN AN INCOMPRESSIBLE VISCOUS FLUID AT VERY HIGH REYNOLDS NUMBERS. *Soviet Physics Uspekhi*, *10*(6), 734

Ramadhan, A., Wagner, G. L., Hill, C., Campin, J.-M., Churavy, V., Besard, T., Souza, A., Edelman, A., Ferrari, R., & Marshall, J. (2020). Oceananigans.jl: Fast and friendly geophysical fluid dynamics on GPUs. Journal of Open Source Software, 5(53), 2018.

Shcherbina, A. Y., D'Asaro, E. A., & Nylund, S. (2018). Observing Finescale Oceanic Velocity Structure with an Autonomous Nortek Acoustic Doppler Current Profiler. *Journal of Atmospheric and Oceanic Technology*, *35*(2), 411–427.

Sreenivasan, K. R. (1995). On the universality of the Kolmogorov constant. *Physics of Fluids*, *7*(11), 2778–2784.

Wiles, P. J., Rippeth, T. P., Simpson, J. H., & Hendricks, P. J. (2006). A novel technique for measuring the rate of turbulent dissipation in the marine environment. *Geophysical Research Letters*, *33*(21).

Acknowledgements

Sam Aucoin would like to thank Professor Makoto Taniguchi (谷口真人) for his supervision during this project and his help in organising the field campaign. Sam Aucoin would also like to thank Professors Makoto Yamada (山田誠) and Shinji Ohsawa (大沢信二) for their assistance during the course of the field study. This project was funded jointly by Mitacs and the Japan Society for the Promotion of Science.